Towards identification of silicon vacancy-related electron paramagnetic resonance centers in 4*H*-SiC

A. Csóré,[1] N. T. Son,[2] and A. Gali[1,3]

[1]*Department of Atomic Physics, Budapest University of Technology and Economics, Budafoki út 8., H-1111 Budapest, Hungary*
[2]*Department of Physics, Chemistry and Biology, Linköping University, SE-58183 Linköping, Sweden*
[3]*Wigner Research Centre for Physics, P.O. Box 49, Budapest H-1525, Hungary*

(Received 9 April 2021; revised 22 June 2021; accepted 7 July 2021; published 26 July 2021)

The negatively charged silicon vacancy (V_{Si}^-) in silicon carbide (SiC) is a paramagnetic and optically active defect in hexagonal SiC. The V_{Si}^- defect possesses $S = 3/2$ spin with long spin coherence time, and it can be optically manipulated even at room temperature. Recently, electron spin resonance signals have been observed besides those associated with the V_{Si}^- defects in the 4*H* polytype of SiC. The corresponding centers share properties akin to those of the V_{Si}^- defects and thus they may be promising candidates for quantum technology applications. However, the exact origin of the new signals is unknown. In this paper, we report V_{Si}^--related pair defect models as possible candidates for the unknown centers. We determine the corresponding electronic structures and magneto-optical properties as obtained by density functional theory calculations. We propose models for the recently observed electron paramagnetic resonance centers, and we predict their optical signals for identification in future experiments.

DOI: 10.1103/PhysRevB.104.035207

I. INTRODUCTION

Paramagnetic point defects in solids have attracted a great deal of attention as they can act as quantum bits (qubits) and single-photon sources, which are the building blocks of quantum technology applications. In particular, point defects embedded in diamond and silicon carbide (SiC) are leading candidates as these hosts provide wide band gaps, allowing a large separation of the deep defect levels with long coherence times.

In particular, the negatively charged silicon vacancy (V_{Si}^-) in silicon carbide (SiC) is one of the most studied defects in hexagonal SiC polytypes. V_{Si}^- defects exhibit an $S = 3/2$ spin state as observed in electron paramagnetic resonance (EPR) experiments [1]. Furthermore, at the single defect level, the ground state exhibits a long spin coherence time and can be optically manipulated even at room temperature [2]. The corresponding optical emission of all V_{Si}^- defects falls into the near-infrared (NIR) region with zero-phonon lines (ZPLs) of 1.438 and 1.352 eV in the 4*H* polytype denoted as V_1 and V_2, respectively [3,4]. These outstanding properties make V_{Si}^- defects highly promising qubits [2,5–15] in ultrasensitive nanosensor applications such as magnetometry [16–21] and thermometry [17,22].

A rich set of data has been accumulated in the past decades from magnetic resonance experiments on V_{Si}^- in 4*H* SiC; however, many details have not yet been resolved. Due to the lattice structure of the 4*H* polytype, two different V_{Si}^- defects can be formed: one is located at a hexagonal lattice site labeled as V_{Si}^--*h* and V_{Si}^--*k* residing at a quasicubic site. In this way, two different photoluminescence (PL) and EPR signals are expected; however, four V_{Si}^--related EPR signals have been observed, labeled as T_{1va}, T_{2va}, T_{1vb}, T_{2vb} [3,23–26], and another two denoted as R_1 and R_2, which have been recently attributed to this family [27]. Common properties of these centers are the $S = 3/2$ ground state, the C_{3v} defect symmetry, the same isotropic *g*-value of 2.0029 [27], and the relatively small zero-field splittings (ZFSs) characterized by the *D* tensor (cf. Table IV). Alternative identifications have been reported for the T_V signals suggesting V_{Si}^0 [28] and V_{Si}^--V_C^0 complex [5,29] defect models, where V_C^0 is located at the third and seventh neighbor along the crystal axis (*c*-axis) [23,25]. Nevertheless, both models have been discredited by recent density functional theory (DFT) calculations [30,31] assigning T_{1va} to V_{Si}^--*h* and T_{2va} to V_{Si}^--*k*, while the other four signals remained unidentified.

Previous EPR measurements were carried out on electron-irradiated 4*H* SiC grown by chemical vapor deposition (CVD) [27]. These measurements were low-doped with a residual *N*-doping concentration of $\approx 5 \times 10^{12}$ cm^{-3} as estimated from the corresponding PL spectrum [32]. The sample preparation technique together with the closely related properties of the unidentified EPR centers to V_{Si}^- suggest that these signals arise from V_{Si}-related intrinsic defect complexes. Our aim is to reveal these defect structures acting as the unidentified EPR centers. To establish the corresponding defect models, it is beneficial to gain knowledge on the formation process of intrinsic defects in SiC. Formation and kinetics of V_{Si} and related defects in 4*H* SiC have already been investigated by DFT and Monte Carlo simulations [33,34]. In a previous work, Defo *et al.* [34] showed that upon implantation of Si^{2+}, a significant amount of interstitial Si and C defects form in addition to silicon and carbon vacancies. Furthermore, Eberlein and co-workers [33] reported that if electron-hole pairs are present during the sample preparation (e.g., upon electron irradiation), then interstitial defects are converted to antisite defects with high probability.

In this work, we employ *ab initio* DFT calculations in order to identify the V_{Si}^{-}-related EPR centers. To this end, we establish defect models as candidates for the reported EPR signals. These models are introduced in Sec. II. The applied methodology is described in Sec. III; in particular, we summarize the utilized computational techniques in Sec. III A, we describe the formulation and the derivation of formation and binding energies in Sec. III B, and parameters of ZFS are introduced in Sec. III C. We present our results in Sec. IV, in particular the corresponding electronic structures in Sec. IV A, defect formation energies in Sec. IV B, and the calculated D constants and ZPLs for all defect models in Sec. IV C. Although EPR centers exhibiting C_{3v} symmetry have been reported, lower symmetry defects can also be formed during the irradiation process used to prepare the experimental samples [27]. Consequently, we dedicate Sec. IV D to discuss the difficulties in resolving the EPR spectrum of defects with C_{1h} symmetry. We conclude our work in Sec. V with a summary of the results.

II. DEFECT MODELS

In this section, we describe the established defect models as candidates for the unidentified EPR centers [27]. Although all these centers exhibit C_{3v} symmetry, defects with lower symmetry (C_{1h}) may also be formed upon irradiation. However, an EPR signal of low-symmetry defects can be extremely challenging to resolve. In this study, we focus mainly on the identification of the C_{3v} centers using axially symmetric defect models introduced in this section. Nevertheless, in Sec. IV D we demonstrate the experimental difficulties in resolving a low-symmetry EPR spectra by employing an exemplary C_{1h} defect model.

Since the four unidentified EPR centers share closely related properties to those of the isolated V_{Si}^{-} defects, they may introduce a similar ground-state electronic structure with the $S = 3/2$ spin state. However, the corresponding spin densities may be slightly modified yielding different D constants (cf. Table IV). Consequently, defect complexes consisting of V_{Si}^{-} and another single defect denoted as X may be suitable candidates for this role, where X is expected to act perturbatively on the electronic structure of V_{Si}^{-}. To preserve the C_{3v} symmetry reported for all EPR centers [27], X should be located along the c-axis establishing axial V_{Si}^{-}-X complexes. Due to the crystal structure of the 4H polytype, if V_{Si}^{-} is located at an h/k site, then X will reside also in an h/k layer along the c-axis. Here we note that such defect models have already been proposed [23,25] following similar arguments. In particular, the V_{Si}^{-}-V_{C}^{0} defect complexes comprising distant V_{Si}^{-} and V_{C}^{0} defects along the c-axis have been suggested [5,29] to be promising candidates; however, the corresponding electronic structure forms the $S = 1/2$ ground state as revealed by earlier DFT calculations [30].

In this work, we investigate defect models involving distant V_{Si}^{-}-X defect pairs coordinated axially in the 4H SiC lattice, where we assign X to the neutral carbon or silicon antisite defects denoted as C_{Si}^{0} and Si_{C}^{0}, respectively, as depicted in Fig. 2. These assignments are supported by the fact that the intrinsic antisites of SiC introduce spinless electronic structures (cf. Fig. 1). In particular, Si_{C}^{0} introduces low-lying fully occupied states, i.e., an a_1 and an e state, to the band gap of 4H SiC, whereas C_{Si}^{0} is electrically inactive. As a consequence, antisite defects would introduce relatively small perturbation to the neighbor V_{Si}^{-} defect, particularly C_{Si}^{0}, thus antisite defects would not alter the spin state of V_{Si}^{-}, but they would modify the corresponding D constants, which are sensitive to the strain caused by the antisite defect.

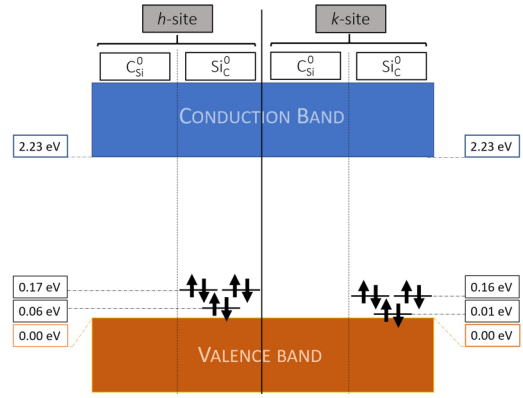

FIG. 1. Kohn-Sham levels introduced by antisites to the band gap of 4H SiC situated at both h and k sites as calculated by PBE functional. Energy levels for Si_{C}^{0} are slightly lower for Si_{C}^{0}-k than for Si_{C}^{0}-h, while no states are located in the band gap either for C_{Si}^{0}-h or for C_{Si}^{0}-k.

III. METHODOLOGY

A. Computational methodology

All investigated defects were modeled in a 576-atom 4H supercell, while for D-constant and ZPL calculations a 1536-atom supercell was also used. Both supercells are sufficiently large, enabling only Γ-point sampling of the Brillouin zone to reach convergent wave functions. Calculations were carried out by using the spin-polarized Heyd-Scuseria-Ernzerhof (HSE06) [35] hybrid functional and the computationally more economical Perdew-Burke-Ernzerhof (PBE) [36] functional. In particular, the electronic structure is described by the HSE06 functional applied on a 576-atom supercell, while for calculations of the magneto-optical properties we employ the PBE functional on a 1536-atom supercell. For defect formation energies, we test both functionals: we report results calculated by the HSE06 functional in Sec. IV B, while PBE results for defect formation energies are reported in Appendix A. Kohn-Sham (KS) wave functions were expanded in a plane-wave basis set with a cutoff energy of 420 eV. In the calculations, only valence electrons were treated explicitly; core-electrons were considered in the framework of the projector augmented wave (PAW) method [37] as implemented in the Vienna Ab-Initio Simulation Package (VASP) [38]. Fully relaxed geometries were obtained by minimizing the forces between the ions falling below the threshold of 0.01 eV/Å.

In addition to the close similarities between the observed EPR centers, their—relatively small—axial component D constants slightly differ, while the orthorhombic component E constants of the corresponding ZFSs are zero for all defects due to the C_{3v} symmetry exhibited by these centers. In this way, unambiguous identification may be achieved by

TABLE I. Heat of formation (δH) of 4H SiC and chemical potential values for Si atom in bulk Si ($\mu_{\rm Si}^{\rm b}$), for the C atom in diamond ($\mu_{\rm C}^{\rm b}$) and for the Si-C pair in 4H SiC ($\mu_{\rm SiC}$) calculated by the HSE06 functional.

Functional	$\mu_{\rm Si}^{\rm b}$ (eV)	$\mu_{\rm C}^{\rm b}$ (eV)	$\mu_{\rm SiC}$ (eV)	δH (eV)
PBE	−5.42	−9.10	−15.06	−0.54

comparing the experimental D constants to those yielded by DFT calculations. To this end, we applied the house-built code as implemented by Ivády *et al.* [39] on PBE wave functions yielded by 576- and 1536-atom supercell calculations. In addition to the EPR signature, the ZPLs may also be very helpful in defect identification. To determine the corresponding ZPLs, we employed 576-atom supercells and calculated the excited state of all defect models employing the ΔSCF method [40,41].

B. Formation and binding energies

The formation energy of the defects provides information about the concentration of the defects under thermodynamical equilibrium conditions. Formation energy may be defined as

$$E_{\rm form}^{q} = E_{\rm tot}^{q} - \frac{n_{\rm Si}+n_{\rm C}}{2}\mu_{\rm SiC} - \frac{\mu_{\rm Si}^{\rm b}-\mu_{\rm C}^{\rm b}-\delta\mu}{2}(n_{\rm Si}-n_{\rm C}) + q(E_{\rm F}+E_{\rm VBM}) + \Delta V(q), \quad (1)$$

where $E_{\rm tot}^{q}$ is the total energy of the defective system in the q charge state, $\mu_{\rm Si}^{\rm b}$, $\mu_{\rm C}^{\rm b}$ are the chemical potentials of the Si atom in bulk Si and the C atom in diamond, respectively, $E_{\rm VBM}$ represents the valence-band edge, and $\Delta V(q)$ stands for the charge-correction term. To determine $\Delta V(q)$, we use the Freysoldt charge-correction scheme [42]. The chemical potential difference of $\delta\mu$ is defined as

$$\delta\mu = (\mu_{\rm Si}-\mu_{\rm C}) - \left(\mu_{\rm Si}^{\rm b}-\mu_{\rm C}^{\rm b}\right), \quad (2)$$

where $\mu_{\rm Si}$ and $\mu_{\rm C}$ are the chemical potentials of the Si and C atoms, respectively, in the SiC lattice obeying the $\mu_{\rm SiC} = \mu_{\rm Si}+\mu_{\rm C}$ relation. The heat of formation (δH) of the Si-C pair in 4H SiC can be defined as

$$\delta H = \mu_{\rm Si}^{\rm b} + \mu_{\rm C}^{\rm b} - \mu_{\rm SiC}. \quad (3)$$

By comparing Eqs. (2) and (3), one finds that $\delta\mu$ is limited by δH, i.e., under an extremely C-rich condition ($\mu_{\rm C} = \mu_{\rm C}^{\rm b}$) $\delta\mu = -\delta H$, while for the Si-rich limit ($\mu_{\rm Si} = \mu_{\rm Si}^{\rm b}$) $\delta\mu = \delta H$, and in the stoichiometric case $\delta\mu = 0$. The corresponding values calculated by the HSE06 functional are listed in Table I.

Since our assumption regarding the defect models is that the $V_{\rm Si}$ defect is in its single negative charge state, it is reasonable to calculate the formation and binding energies within the region between the (0/−) and (−/2−) adiabatic charge transition levels of the $V_{\rm Si}$ defects. The adiabatic charge transition levels can be derived from Eq. (1) as follows:

$$E_{q+1/q} = E_{\rm tot}^{q} - E_{\rm tot}^{q+1} + \Delta V(q) - \Delta V(q+1). \quad (4)$$

In this work, we study defect complexes that may form randomly in the cascade process upon irradiation on SiC. The relative stability of isolated $V_{\rm Si}$ with respect to the complexes of $V_{\rm Si}^{-}$ with X can be studied by the binding energy ($E_{\rm b}$) between the constituting species as

$$E_{\rm b}(E_{\rm F}) = E_{\rm form}^{V_{\rm Si}^{-}}(E_{\rm F}) + E_{\rm form}^{X}(E_{\rm F}) - E_{\rm form}^{V_{\rm Si}^{-}\text{-}X}(E_{\rm F}), \quad (5)$$

where $E_{\rm form}^{V_{\rm Si}^{-}}(E_{\rm F})$, $E_{\rm form}^{X}(E_{\rm F})$, and $E_{\rm form}^{V_{\rm Si}^{-}\text{-}X}(E_{\rm F})$ are the formation energies of $V_{\rm Si}^{-}$, X, and $V_{\rm Si}^{-}$-X as a function of the Fermi level ($E_{\rm F}$), respectively. According to this definition, $E_{\rm b} > 0$ implies that the dissociation $V_{\rm Si}^{-}$-X complex is an endothermic process.

C. Zero-field splitting parameters for $S = 3/2$ systems

Zero-field splitting (ZFS) of energy levels manifests in systems with $S \geqslant 1$ spin. The corresponding Hamiltonian reads

$$\hat{H}_{\rm ss} = \hat{\mathbf{S}}^{\top}\mathbf{D}\hat{\mathbf{S}}, \quad (6)$$

where $\hat{\mathbf{S}} = \sum_i \hat{\mathbf{S}}_i$ is the total spin operator obtained as the superposition of the $\hat{\mathbf{S}}_i$ one-particle spin operators. In Eq. (6), the ZFS tensor in represented by $\mathbf{D}$, and using its diagonalized form, the spin-spin Hamiltonian takes the form

$$\hat{H}_{\rm ss} = D_{xx}\hat{S}_x^{\,2} + D_{yy}\hat{S}_y^{\,2} + D_{zz}\hat{S}_z^{\,2}, \quad (7)$$

where D_{ij} are elements of the $\mathbf{D}$-tensor, and $\hat{S}_x$, $\hat{S}_y$, and $\hat{S}_z$ are the components of $\hat{\mathbf{S}}$ in the x, y, and z directions, respectively.

Introducing the D and E ZFS parameters, i.e., the respective axial and orthorhombic components, the eigenvalue of $\hat{H}_{\rm ss}$ ($E_{\rm ss}$) can be written as

$$E_{\rm ss} = D\left(m_S^2 - \frac{S(S+1)}{3}\right) + E\left(S_x^2 + S_y^2\right), \quad (8)$$

where we use that the eigenvalue of $\hat{\mathbf{S}}^{\mathbf{2}}$ is $S(S+1)$, with S being the eigenvalue of $\hat{\mathbf{S}}$, and the eigenvalues of $\hat{S}_x$, $\hat{S}_y$, and $\hat{S}_z$ are S_x, S_y, and m_S, respectively. The ZFS parameters can be expressed as $D = 3D_{zz}/2$ and $E = (D_{yy} - D_{xx})/2$. Under C_{3v} symmetry, the $\mathbf{D}$-tensor contains two principal values, i.e., $D_{xx} = D_{yy}$ and D_{zz}, and hence the orthorhombic term is zero, $E = 0$, simplifying Eq. (8) to

$$E_{\rm ss} = D\left(m_S^2 - \frac{S(S+1)}{3}\right). \quad (9)$$

In our calculations, the spin quantization axis, i.e., the z-axis, is aligned with the c-axis and $S = \frac{3}{2}$ for the investigated defects, implying $m_S = \{\pm\frac{3}{2}, \pm\frac{1}{2}\}$. The corresponding eigenvalues are $-D$ for $m_S = \pm 1/2$ and D for $m_s = \pm 3/2$ states, implying the splitting of $2D$ between the spin levels.

We calculated the matrix elements of the $\mathbf{D}$-tensor as implemented by Ivády *et al.* [39]. The corresponding elements can be calculated as [39,43]

$$D_{kl} = \frac{\mu_0\mu_{\rm B}^2 g_0^2}{S(2S-1)}\sum_{i<j}^{n}\chi_{ij}\iint \rho^{(2)}(\boldsymbol{r}_1,\mathbf{r}_2) \times \left(\frac{|\boldsymbol{r}_2-\boldsymbol{r}_1|^2\delta_{kl} - 3(\boldsymbol{r}_2-\boldsymbol{r}_1)_k\cdot(\boldsymbol{r}_2-\boldsymbol{r}_1)_l}{|\boldsymbol{r}_2-\boldsymbol{r}_1|^5}\right)d\boldsymbol{r}_1 d\boldsymbol{r}_2, \quad (10)$$

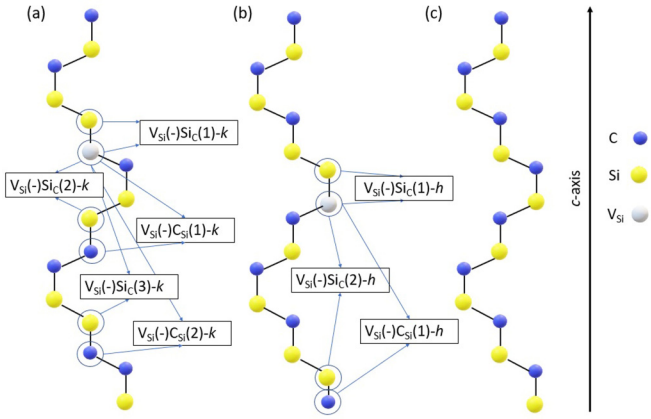

FIG. 2. Defect models of axial V_{Si}^{-}-X defect complexes, where $X = \{C_{Si}^{0}, Si_C^{0}\}$. Neighboring order between V_{Si}^{-} and X are indicated in brackets. The possible (a) V_{Si}^{-}-X-k and (b) V_{Si}^{-}-X-h pair defects along with the (c) perfect lattice are illustrated. Labels of atoms and the c-axis are indicated.

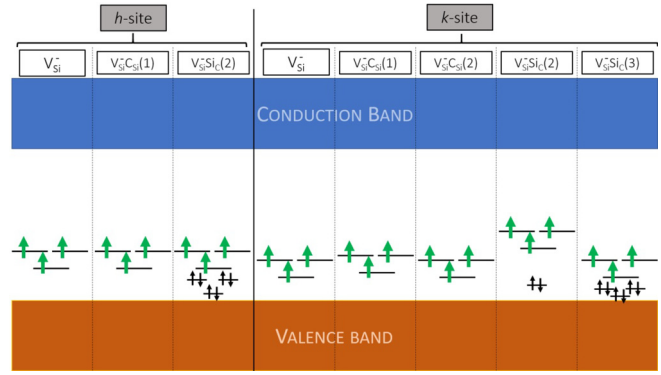

FIG. 3. Electronic structure of all investigated defect models. Notations of defects are aligned with those in Fig. 2. Green arrows represent the electrons of V_{Si}^{-} defects residing at open orbitals, i.e., the active space of the electronic structure. Black arrows stand for electrons at closed energy levels introduced by Si_C^{0}. Valence and conduction bands of 4H SiC are also indicated.

where the constants of μ_0, μ_B, and g_0 are the vacuum permeability, the Bohr-magneton, and the free-electron g-factor, respectively. The summation goes over every pair of occupied Kohn-Sham states, and χ_{kl} is $+1$ for parallel and -1 for antiparallel spins. The integral generates the expectation value of the dipole momentum operator on the two-particle electron density of $\rho^{(2)}(\mathbf{r}_1, \mathbf{r}_2)$ depending on the positions of the two electrons, $\mathbf{r}_1$ and $\mathbf{r}_2$.

IV. RESULTS AND DISCUSSION

In this section, we provide our numerical results for all defect models depicted in Fig. 2. In particular, we report our results about the electronic structure (Sec. IV A), defect formation (Sec. IV B), and the magneto-optical parameters (Sec. IV C).

A. Electronic structure

Geometry relaxation revealed that the formation of V_{Si}^{-} with the nearest neighbor Si_C^{0} is highly unlikely. Instead, they recombine yielding V_C^{-} at both h and k sites. The electronic structure of V_C^{-} is significantly different from that of V_{Si}^{-}; in particular, it introduces the $S = 1/2$ ground state and already identified EPR centers in 4H SiC [44]. Thus, in this context, we exclude the defect model of the V_{Si}^{-} with Si_C^{0} located at the nearest-neighbor C site.

Electronic structures for the investigated defect complexes are illustrated in Fig. 3. Accordingly, isolated V_{Si}^{-} defects at both h and k sites introduce a_1 and e levels into the band gap of 4H SiC, and both of them are half-filled establishing a high-spin state of $S = 3/2$, as already known from previous studies. Introducing C_{Si}^{0} to the system, the electronic structure remains very similar regardless of the neighboring order, i.e., the distance between V_{Si}^{-} and C_{Si}^{0}. In particular, changing in the KS energy levels with respect to those of V_{Si}^{-} defects is $\leqslant$0.05 eV. On the other hand, when Si_C^{0} is included, additional—fully occupied—KS level(s) appear in the band gap near the valence-band minimum (VBM). The electronic structure of V_{Si}^{-}-h with second neighboring Si_C^{0} is akin to that of V_{Si}^{-}-k with third neighboring Si_C^{0}, i.e., fully occupied a_1 and e levels related to Si_C^{0} appear below the half-occupied V_{Si}^{-} orbitals. The positions of the half-occupied levels are close to those of the isolated V_{Si}^{-}, whereas the levels of the fully occupied states are very similar to those of Si_C^{0}. This implies that V_{Si}^{-}-h and Si_C^{0} establish their electronic structures almost independently, i.e., their interaction is negligible. In contrast, for V_{Si}^{-}-k with second-neighbor Si_C^{0}, the change in the electronic structure with respect to either the isolated V_{Si}^{-}-k defect or the isolated Si_C^{0} defect is significant. In particular, KS orbitals of V_{Si}^{-} are pushed up by about 0.3 eV, whereas only one fully occupied a_1 level appears higher by about 0.1 eV than that of the isolated Si_C^{0}-k. Furthermore, no fully occupied e level emerges in the band gap. This significant effect implies that V_{Si}^{-}-k and Si_C^{0}-k cannot be treated individually in this case, i.e., Si_C^{0}-k may not be the only perturbation on V_{Si}^{-}-k. To study the interaction between V_{Si}^{-}-k and Si_C^{0}-k in detail, we derive the corresponding defect-molecule diagram as depicted in Fig. 4. Accordingly, KS states in the band gap are built up as a combination of the symmetry-linked orbitals of V_{Si}^{-}-k and Si_C^{0}-k, i.e., these states belong to both defects. Localization of the corresponding spin density is illustrated in Fig. 5, where we show also the spin density of the isolated V_{Si}^{-}-k for comparison. In particular, the spin density corresponding to the V_{Si}^{-}-$Si_C^{0}(2)$-k complex significantly spreads towards Si_C^{0}-k [cf. Fig. 5(d)]. In contrast, for the isolated V_{Si}^{-}-k [cf. Fig. 5(c)] there is a negligible contribution of the spin density on the C atom that is replaced by the Si atom in the V_{Si}^{-}-Si_C^{0}-k defect complex. As a result, the corresponding D constant may significantly differ from the observed values listed in Table IV. Indeed, we obtain the D constant value of 173.87 MHz for this defect complex, which is one order of magnitude larger than the experimental values for the unknown EPR centers. This further supports that Si_C^{0}-k at the second-neighbor C-site of V_{Si}^{-} cannot be treated as only a weak perturbation on the electronic structure of V_{Si}^{-}, and hence we exclude this defect model from further investigations in this context.

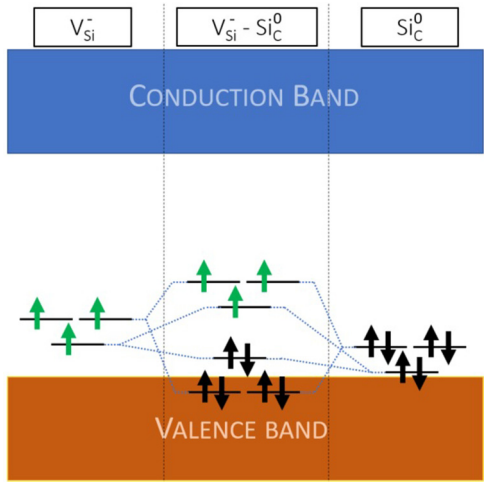

FIG. 4. A combination of the orbitals of V_{Si}^--k and Si_C^0-k yielding mixed states, particularly fully occupied e and a_1 states, where the e level falls into the valence band (VB). The fully occupied a_1 state and, in addition, the half-occupied a_1 and e states lie in the band gap. Green arrows stand for the unpaired electrons establishing the spin density [orange lobes in Fig. 5(d)], whereas black arrows represent the paired electrons.

B. Defect formation

To determine the binding energies of the V_{Si}^--X complexes, we calculated the formation energies as functions of the Fermi level using the introduced defect models reported in Sec. II. Since EPR signatures of V_{Si}^--h/k are observed in the corresponding experimental spectra [27], we calculated the formation and binding energies within the Fermi level region, where V_{Si}^--h/k is stable, i.e., between the $(0/-)$ and $(-/2-)$ charge transition levels of V_{Si}^--h/k. Furthermore, we also assume that C_{Si} and Si_C are in their neutral charge state, i.e., $q = 0$ within this region, implying that the last two terms in Eq. (1) vanish for these defects. Charge transition levels of V_{Si}^--h/k calculated by the HSE06 functional are reported in Table II. We note that similar values are reported for the S1 and S2 deep-level transient spectroscopy (DLTS) centers [45], which are later identified as V_{Si}^- [46,47]. Further values for charge transition levels calculated by DFT were reported in Refs. [34,48,49].

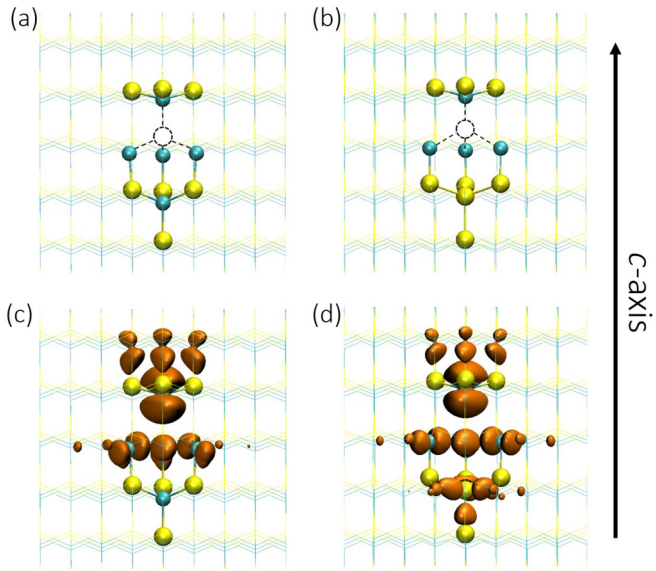

FIG. 5. Defect structure of (a) V_{Si}^--k and (b) V_{Si}^--Si_C^0-k and the corresponding charge densities established by electrons in the majority spin channel (orange lobes) generated by using the same isovalues, (c) and (d), respectively. The supercell structure is shown in orthographic view and the lattice is represented by a wire structure. In the core of the defects, Si and C atoms are represented by yellow and cyan balls, respectively, while dashed balls stand for the V_{Si}.

TABLE II. Values for the $(0/-)$ and $(-/2-)$ charge transition levels of V_{Si}^--h/k defects in 4H SiC as calculated by the HSE06 functional. All values are referenced to the valence-band maximum.

Functional	Defect	$E_{(0/-)}$ (eV)	$E_{(-/2-)}$ (eV)
HSE06	V_{Si}^--h	1.29	2.59
	V_{Si}^--k	1.26	2.47

Formation energies as a function of the Fermi-level for the isolated defect species under stoichiometric conditions are reported in Table III and depicted for the hexagonal defects in Fig. 6. We note that similar values were obtained from previous local spin density approximation DFT calculations [48,49]. Based on the numerical results, V_{Si}^- defects exhibit the largest formation energy across the investigated Fermi-energy region. Formation energies of V_{Si}^--C_{Si} defect complexes are higher by about 0.1 eV than those of V_{Si}^--Si_C defect complexes.

Based on the calculated formation energies, we calculated the binding energies of the corresponding V_{Si}^--X defect complexes by using Eq. (5). Since both $\delta\mu$ and E_F are canceled out, all defect complexes exhibit constant binding energy values across the investigated E_F region, and they are also insensitive to the chemical environment. The obtained values are listed in Table III. Generally, all defect models exhibit small binding energies, supporting the idea that the presence of the X defect species is indeed a perturbation for V_{Si}^- establishing only weakly bound complexes. Since the binding energies are close to each other for the different V_{Si}^--X

TABLE III. Formation (E_{form}) and binding energies (E_b) of the V_{Si}^--X defect complexes calculated HSE06 functional in the Fermi-level (E_F) region between the $(0/-)$ and $(-/2-)$ charge transition levels of V_{Si}-h/k under stoichiometric conditions.

Defect	E_{form} (eV)	E_b (eV)
V_{Si}^--h	$7.45 - E_F$	
V_{Si}^--k	$7.47 - E_F$	
C_{Si}-h	4.27	
C_{Si}-k	4.23	
Si_C-h	4.06	
Si_C-k	4.03	
V_{Si}^--$C_{Si}(1)$-h	$11.49 - E_F$	0.23
V_{Si}^--$Si_C(2)$-h	$11.38 - E_F$	0.14
V_{Si}^--$C_{Si}(1)$-k	$11.46 - E_F$	0.24
V_{Si}^--$C_{Si}(2)$-k	$11.46 - E_F$	0.24
V_{Si}^--$Si_C(3)$-k	$11.34 - E_F$	0.15

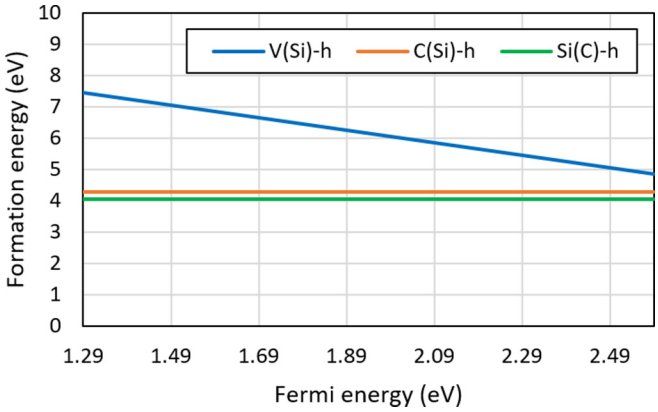

FIG. 6. Formation energies of isolated V_{Si}, C_{Si}, and Si_C defects under stoichiometric conditions calculated by the HSE06 functional in the Fermi-level region between the $(0/-)$ and $(-/2-)$ charge transition levels of V_{Si}-h/k.

complexes, they may appear in the same order of magnitude concentration in irradiated and annealed 4*H* SiC.

C. Magneto-optical signatures

All V_{Si}^--*X* defect complexes introduce a similar spin-3/2 electronic structure to that of the isolated V_{Si}^- defects, i.e., the $^4A_2$ ground state. The paramagnetic ground state makes them EPR-active centers, and thus their signals may appear besides that of the isolated V_{Si}^- defects. Indeed, several signals have been observed recently, labeled as T_{V1b}, T_{V2b}, R_1, and R_2 [3,23–27], exhibiting similar spin properties to those of the T_{V1a} and T_{V2a} centers previously assigned to V_{Si}^--*h* and V_{Si}^--*k*, respectively [30,31]. Here we note that the orthorhombic parameter of the ZFS, i.e., the *E* constant, is zero for all the experimentally reported signals, indicating that the centers exhibit C_{3v} symmetry. The corresponding experimental ZFS *D*-constants are listed in Table IV, while in Table V we report our numerical values obtained by means of the PBE functional applied on 576- and 1536-atom supercells. Accordingly, numerical values for the isolated V_{Si}^- agree with the previously reported ones, which also resulted from DFT calculations [30,31]. Regarding the V_{Si}^--*X* defects, all calculated *D* values fall into the 18–34 MHz region for both supercell sizes but for the V_{Si}^--C_{Si}-*k* defect, where the corresponding *D* constant is one order of magnitude lower. This might be because the distance between the V_{Si}^- and C_{Si} defect species is the shortest, and hence the presence of C_{Si} has the largest effect on the spin density of V_{Si}^- among the other defect complexes (see Fig. 2). Here we note that the distance between V_{Si}^- and Si_C antisite in the V_{Si}^--$Si_C(2)$-*k* defect model is even shorter; however, it is already excluded from our recent scope (see Sec. IV A). A similar trend can be observed in the experimental signals

TABLE IV. Experimental values for ZFS *D* constants of the EPR signals reported in Ref. [27].

Signal	T_{V1a}	T_{V2a}	T_{V1b}	T_{V2b}	R_1	R_2
D_{exp} (MHz)	2.50	35.0	32.6	20.0	2.24	39.4

TABLE V. Calculated values for ZFS *D* constants of the isolated V_{Si}^- defects and the V_{Si}^--*X* defect models. The calculated values as obtained by the PBE functional on 576- and 1536-atom supercells are denoted by D_{PBE}^{576} and D_{PBE}^{1536}, respectively.

Defect	D_{PBE}^{576} (MHz)	D_{PBE}^{1536} (MHz)
V_{Si}^--*h*	18.01	15.23
V_{Si}^--$C_{Si}(1)$-*h*	25.56	23.03
V_{Si}^--$Si_C(2)$-*h*	18.75	21.34
V_{Si}^--*k*	24.99	34.19
V_{Si}^--$C_{Si}(1)$-*k*	2.79	2.29
V_{Si}^--$C_{Si}(2)$-*k*	23.92	29.41
V_{Si}^--$Si_C(3)$-*k*	33.57	33.55

where all *D* constants of the unknown centers fall within the 20–40 MHz interval but for the R_1 center exhibiting a one order of magnitude lower *D* constant. As a consequence, we attribute the R_1 signal to the V_{Si}^--C_{Si}-*k* defect. We cannot unambiguously identify the other unknown EPR centers based solely on the calculated *D* constants.

The optical signature of point defects provides additional fingerprints in defect identification. Although fluorescence centers associated with these EPR centers have not yet been reported, we calculated the ZPL energies for the isolated V_{Si}^- defects and for all investigated defect complexes as listed in Table VI. For V_{Si}^- defects, the experimental ZPL energies are 1.438 eV for the V1 (T_{V1a} in EPR) and 1.352 eV for the V2 (T_{V2a} in EPR) PL centers, identified as V_{Si}^--*h* and V_{Si}^--*k*, respectively [30,31]. The lowest and largest ZPL energies are found for V_{Si}^--Si_C-*h* and V_{Si}^--C_{Si}-*k* defects, respectively. The calculated optical signals may be detected in future experiments, which may lead to the identification of the considered defect complexes.

D. EPR of defect complexes exhibiting C_{1h} symmetry

Axial V_{Si}^--*X* pair defects have been investigated so far, but the formation of basal defect configurations exhibiting C_{1h} symmetry is also possible during the cascade process of ion collisions induced by irradiation. Indeed, in the corresponding EPR spectrum [27], several signals of basal centers have been

TABLE VI. Positions of ZPLs for the investigated V_{Si}^--*X* defect models calculated by means of the PBE functional. We also report the values yielded by the HSE06 functional for the isolated V_{Si}^- defects. The ZPL values in the HSE06* column for the defect complexes were obtained by correcting the corresponding PBE result with the difference of the isolated V_{Si}^--related PBE and HSE06 ZPL values as an estimate.

Defect	E_{ZPL}^{PBE} (eV)	E_{ZPL}^{HSE06*} (eV)
V_{Si}^--*h*	1.273	1.450
V_{Si}^--$C_{Si}(1)$-*h*	1.267	1.444
V_{Si}^--$Si_C(2)$-*h*	1.107	1.284
V_{Si}^--*k*	1.198	1.385
V_{Si}^--$C_{Si}(1)$-*k*	1.345	1.532
V_{Si}^--$C_{Si}(2)$-*k*	1.182	1.369
V_{Si}^--$Si_C(3)$-*k*	1.280	1.467

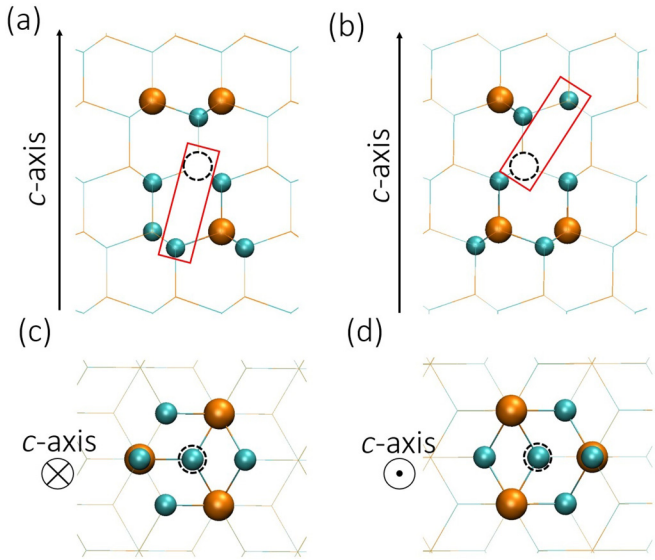

FIG. 7. Defect structures of the investigated basal (a)–(c) V_{Si}^{-}-C_{Si}-$hk^{(a)}$ and (b)–(d) V_{Si}^{-}-C_{Si}-$hk^{(b)}$ defect configurations. The supercell structure is shown in an orthographic view, and the lattice is represented by a wire structure. In the core of the defects, Si and C atoms are represented by orange and cyan balls, respectively, while dashed balls stand for the V_{Si}. We indicate the c-axis for all views.

observed. However, resolving these signals can be extremely challenging because of the emerging orthorhombic ZFS parameter E with the complex angle dependence of the spectrum as a function of the direction external magnetic field direction. Furthermore, various overlapping EPR signals appear to be caused by the different configurations of pair defects.

To demonstrate the complexity of the problem, we consider here two representative basal plane V_{Si}^{-}-C_{Si} configurations. These configurations are obtained by placing C_{Si} in the second-neighbor site with respect to V_{Si}-h. There are two possible defect structures: (a) C_{Si} is the neighbor of the C dangling bond residing off the symmetry axis of the defect [see Fig. 7(a)], and (b) C_{Si} is the neighbor of the C dangling bond residing in the symmetry axis of the defect [see Fig. 7(b)]. These configurations are labeled as V_{Si}^{-}-C_{Si}-$hk^{(a)}$ and V_{Si}^{-}-C_{Si}-$hk^{(b)}$, respectively. Since the C antisite is placed in the second nearest-neighbor site of V_{Si}, the corresponding geometries are severely distorted, as depicted in Fig. 8. The large difference between the geometry of the isolated V_{Si} [see Fig. 8(a)] and that of the investigated basal defects [see Figs. 8(b) and 8(c)] may imply a significant difference

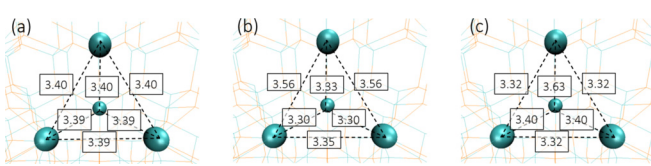

FIG. 8. Distortion of the tetrahedron formed by the 4 × C neighboring the V_{Si} for (a) isolated V_{Si}^{-}-h, (b) V_{Si}^{-}-C_{Si}-$hk^{(a)}$, and (c) V_{Si}^{-}-C_{Si}-$hk^{(b)}$. The 4 × C nuclei are represented by cyan balls, while the rest of the supercell is shown as a wire structure. The bond lengths are given in Å units.

between the respective spin densities governing the ZFS D and E parameters. The ZFS parameters of the basal V_{Si}-related defects may deviate strongly from those of the isolated V_{Si}^{-}-h. Indeed, the respective calculated ZFS parameters are $D^{(a)} = -262.26$ MHz, $E^{(a)} = -20.66$ MHz and $D^{(b)} = -295.64$, MHz $E^{(b)} = -59.36$ MHz. The angle of the principal axis of the D-tensor makes ≈0.8° and ≈70.6° angles with the c-axis, respectively. This large difference between the angles is due to the position of C_{Si}, i.e., for V_{Si}-C_{Si}-$hk^{(a)}$ the C_{Si} is located closer to the symmetry axis of V_{Si} than that for V_{Si}-C_{Si}-$hk^{(b)}$, which implies a smaller deviation from the C_{3v} symmetry for the (a) configuration than that for the (b) configuration. As a result, principal axes of the D-tensor exhibit a small tilt from the c-axis for V_{Si}-C_{Si}-$hk^{(a)}$. The corresponding D constants are at least one order of magnitude higher than those for the reported axial V_{Si}^{-}-X defects (see Table V) as a result of the C_{Si} being closer to the V_{Si}^{-} than X in any of the investigated axial V_{Si}-X complexes, which significantly modifies the spin density matrix of V_{Si}^{-}.

Here we provide simulated EPR spectra of two representative basal V_{Si}^{-}-C_{Si} pair defects (see Fig. 9) modeled in a 576-atom supercell. By using the calculated D-tensors, we simulated the ZFS as a function of the angle of rotation about the $(1\bar{1}00)$ and $(11\bar{2}0)$ axes. Under the condition of $\mathbf{B} \parallel c$, the corresponding splittings are 1048.4 MHz for V_{Si}^{-}-C_{Si}-$hk^{(a)}$ and 713.9 MHz for V_{Si}^{-}-C_{Si}-$hk^{(b)}$. The (a) configuration shows such an angular dependence in the EPR spectrum where the corresponding EPR transition energies are closely grouped; however, the (b) configuration exhibits rather a complicated pattern with split lines in the EPR spectrum as a result of the stronger C_{1h} field originating from C_{Si}. In experiments, both defects that are manifested in the EPR spectrum may be present. Overlaying the two spectra results in a complex pattern that makes it extremely difficult to apply a spin Hamiltonian retrofit to distinguish these two centers. In experiments, other defect configurations produce other complex patterns with various D-tensors of scattering orthorhombic E components, which makes the discrimination of the EPR transition energies associated with different defect configurations almost impossible.

V. SUMMARY

In summary, we carried out DFT calculations in order to identify the recently observed EPR centers [27] possibly associated with V_{Si}^{-} defects in 4H SiC. We set up the corresponding defect models that are complexes exhibiting C_{3v} symmetry and are built up from a V_{Si}^{-} and a farther antisite, i.e., C_{Si} or Si_C along the c-axis in the 4H SiC lattice establishing V_{Si}^{-}-X complexes. We reported the electronic structures revealing that no further states appear in the band gap for $X = C_{Si}$, while for $X = Si_C$ fully occupied levels appear below those of V_{Si}^{-}. In particular, we found that the V_{Si}^{-}-$Si_C(2)$-k defect complex introduces a significantly different electronic structure and spin density with respect to that of the isolated V_{Si}^{-} yielding a one order of magnitude larger D constant than the experimentally observed values.

We also investigated the formation of the defect complexes and found negligible variation in their binding energies, implying defect formation with nearly the same concentrations

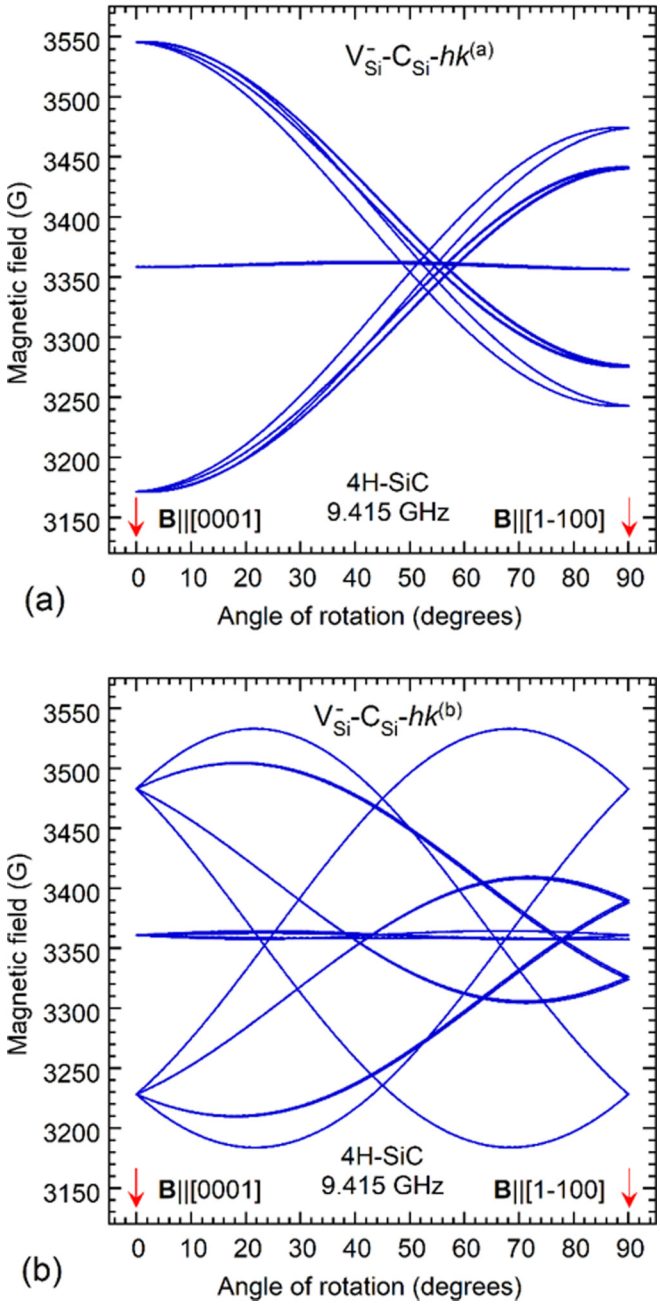

FIG. 9. Angular dependencies of the two representative V_{Si}-related centers in 4*H* SiC with C_{1h} symmetry (a) V_{Si}-C_{Si}-$hk^{(a)}$ and (b) V_{Si}-C_{Si}-$hk^{(b)}$ with the magnetic field rotating in the $(11\bar{2}0)$ plane and the microwave frequency of 9.415 GHz. In the simulations, the *g*-value of the negative Si vacancy ($g = 2.0029$) is assumed for these $S = 3/2$ centers. The fine-structure parameters for the centers are $D^{(a)} = -226.26$ MHz, $E^{(a)} = -20.66$ MHz, and $D^{(b)} = -295.64$ MHz, $E^{(b)} = -59.36$ MHz are from the calculations of the ZFS tensor where the direction of the axial component has an angle of about 0.8° and 70.6°, respectively, with the *c*-axis of 4*H* SiC.

for all the defects. We calculated the ZFS *D*-constants and compared them to the experimental values, which imply that the V_{Si}^{-}-C_{Si}-*k* defect is the origin of the R_1 EPR signal. Although experimental optical spectra are not available in the literature, we also reported the respective ZPL values that—along with future fluorescence or optically detected magnetic resonance measurements—might contribute to unambiguous identification.

TABLE VII. Heat of formation (δH) of 4*H* SiC and chemical potential values for the Si atom in bulk Si (μ_{Si}^{b}), for the C atom in diamond (μ_{C}^{b}), and for the Si-C pair in 4*H* SiC (μ_{SiC}) calculated by the PBE functional.

μ_{Si}^{b} (eV)	μ_{C}^{b} (eV)	μ_{SiC} (eV)	δH (eV)
−5.42	−9.10	−15.06	−0.54

ACKNOWLEDGMENTS

The support from the ÚNKP-20-4 New National Excellence Program of the Ministry for Innovation and Technology from the source of the National Research, Development and Innovation Fund is acknowledged by A.Cs. We acknowledge the support from the BME IE-NAT TKP2020 grant of NKFIH, Hungary. We acknowledge the EU H2020 project QuanTELCO (Grant No. 862721). A.G. acknowledges the Hungarian National Quantum Technology Program (Grant No. 2017-1.2.1-NKP-2017-00001), the QuantERA project Nanospin (Grant No. NN127902), and the support from the Quantum Information National Laboratory from the Ministry for Innovation and Technology. N.T.S. acknowledges the Swedish Research Council (Grant No. VR 2016-04068) and the Knut and Alice Wallenberg Foundation (Grant No. KAW 2018.0071). We acknowledge the computational sources provided by the Swedish National Infrastructure for Computing (SNIC) at the National Computation Centre (NSC) partially funded by the Swedish Research Council through grant agreement No. 2018-05973 and the Governmental Agency for IT Development of Hungary through the project "gallium."

APPENDIX A: NUMERICAL RESULTS FOR THE FORMATION OF $V_{Si}(-)$-*X* COMPLEXES BY MEANS OF PBE FUNCTIONAL

We calculated the formation and binding energies for the V_{Si}^{-}-*X* axial complexes also with the PBE [36] functional. Here we report these results for comparison with that yielded by the HSE06 functional. In Table VII we present the parameters for the formation energy calculations, i.e., for Eq. (1).

(0/−) and (−/2−) charge transition levels of V_{Si} defects—designating the Fermi-level region for the formation and binding energies—are presented in Table VIII.

Accordingly, results yielded by PBE functionals are lower by about 0.6–0.7 eV for the (0/−) level and by about 0.9–1.0 eV for (−/2−) level than those obtained by the HSE06

TABLE VIII. Values for the (0/−) and (−/2−) charge transition levels of V_{Si}^{-}-*h*/*k* defects in 4*H* SiC as calculated by the PBE functional. All values are referenced to the valence-band maximum.

Defect	$E_{(0/-)}$ (eV)	$E_{(-/2-)}$ (eV)
V_{Si}^{-}-*h*	0.64	1.58
V_{Si}^{-}-*k*	0.57	1.60

TABLE IX. Formation (E_{form}) and binding energies (E_{b}) of the V_{Si}^{-}-X defect complexes calculated PBE functional in the Fermi-level (E_{F}) region between the $(0/-)$ and $(-/2-)$ charge transition levels of V_{Si}-h/k under stoichiometric condition.

Defect	E_{form} (eV)	E_{b} (eV)
V_{Si}^{-}-h	$7.05 - E_{\text{F}}^{\text{PBE}}$	
V_{Si}^{-}-k	$7.06 - E_{\text{F}}^{\text{PBE}}$	
C_{Si}-h	3.43	
C_{Si}-k	3.39	
Si_C-h	3.96	
Si_C-k	4.00	
V_{Si}^{-}-$C_{Si}(1)$-h	$10.46 - E_{\text{F}}$	0.02
V_{Si}^{-}-$Si_C(2)$-h	$11.08 - E_{\text{F}}$	−0.07
V_{Si}^{-}-$C_{Si(1)}$-k	$10.41 - E_{\text{F}}$	0.04
V_{Si}^{-}-$C_{Si}(2)$-k	$10.41 - E_{\text{F}}$	0.03
V_{Si}^{-}-$Si_C(3)$-k	$11.04 - E_{\text{F}}$	0.02

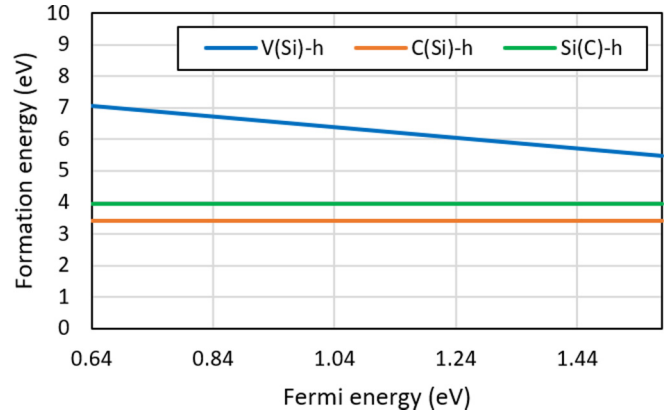

FIG. 10. Formation energies of isolated V_{Si}, C_{Si}, and Si_C defects under stoichiometric conditions calculated by the PBE functional in the Fermi-level region between the $(0/-)$ and $(-/2-)$ charge transition levels of V_{Si}-h/k.

functional listed in Table II. On the other hand, both functionals predict that both charge transition levels lie higher for V_{Si}^{-}-h than those for V_{Si}^{-}-k.

Formation energies for the V_{Si}^{-}-X defect complexes are listed in Table IX and depicted in Fig. 10. Values for V_{Si}^{-}-C_{Si} defect models are lower by about 0.6 eV than those for the V_{Si}^{-}-Si_C defect complexes. Generally, all formation energy values calculated by means of the HSE06 functional (cf. Table III) are higher than the PBE ones. However, the HSE06 functional predicts one order of magnitude larger binding energies—and thus higher stability—for all defect models other than those calculated by the PBE functional.

[1] T. Wimbauer, B. K. Meyer, A. Hofstaetter, A. Scharmann, and H. Overhof, Phys. Rev. B **56**, 7384 (1997).

[2] M. Widmann, S.-Y. Lee, T. Rendler, N. T. Son, H. Fedder, S. Paik, L.-P. Yang, N. Zhao, S. Yang, I. Booker, A. Denisenko, M. Jamali, S. A. Momenzadeh, I. Gerhardt, T. Ohshima, A. Gali, E. Janzén, and J. Wrachtrup, Nat. Mater. **14**, 164 (2015).

[3] E. Sörman, N. T. Son, W. M. Chen, O. Kordina, C. Hallin, and E. Janzén, Phys. Rev. B **61**, 2613 (2000).

[4] R. Nagy, M. Niethammer, M. Widmann, Y.-C. Chen, P. Udvarhelyi, C. Bonato, J. U. Hassan, R. Karhu, I. G. Ivanov, N. T. Son, J. R. Maze, T. Ohshima, n. O. Soykal, d. Gali, S.-Y. Lee, F. Kaiser, and J. Wrachtrup, Nat. Commun. **10**, 1 (2019).

[5] H. Kraus, V. A. Soltamov, D. Riedel, S. Väth, F. Fuchs, A. Sperlich, P. G. Baronov, V. Dyakonov, and G. V. Astakhov, Nat. Phys. **10**, 157 (2014).

[6] P. G. Baranov, A. P. Bundakova, A. A. Soltamova, S. B. Orlinskii, I. V. Borovykh, R. Zondervan, R. Verberk, and J. Schmidt, Phys. Rev. B **83**, 125203 (2011).

[7] D. Riedel, F. Fuchs, H. Kraus, S. Väth, A. Sperlich, V. Dyakonov, A. A. Soltamova, P. G. Baranov, V. A. Ilyin, and G. V. Astakhov, Phys. Rev. Lett. **109**, 226402 (2012).

[8] V. A. Soltamov, A. A. Soltamova, P. G. Baranov, and I. I. Proskuryakov, Phys. Rev. Lett. **108**, 226402 (2012).

[9] F. Fuchs, B. Stender, M. Trupke, D. Simin, J. Pflaum, V. Dyakonov, and G. V. Astakhov, Nat. Commun. **6**, 7578 (2015).

[10] F. Fuchs, V. A. Soltamov, S. Väth, P. G. Baranov, E. N. Mokhov, G. V. Astakhov, and V. Dyakonov, Sci. Rep. **3**, 1637 (2013).

[11] S. G. Carter, O. O. Soykal, P. Dev, S. E. Economou, and E. R. Glaser, Phys. Rev. B **92**, 161202(R) (2015).

[12] O. O. Soykal, P. Dev, and S. E. Economou, Phys. Rev. B **93**, 081207(R) (2016).

[13] D. Simin, H. Kraus, A. Sperlich, T. Ohshima, G. V. Astakhov, and V. Dyakonov, Phys. Rev. B **95**, 161201(R) (2017).

[14] M. Radulaski, M. Widmann, M. Niethammer, J. L. Zhang, S.-Y. Lee, T. Rendler, K. G. Lagoudakis, N. T. Son, E. Janzén, T. Ohshima, J. Wrachtrup, and J. Vučković, Nano Lett. **17**, 1782 (2017).

[15] R. Nagy, M. Widmann, M. Niethammer, D. B. R. Dasari, I. Gerhardt, O. O. Soykal, M. Radulaski, T. Ohshima, J. Vučković, N. T. Son, I. G. Ivanov, S. E. Economou, C. Bonato, S.-Y. Lee, and J. Wrachtrup, Phys. Rev. Appl. **9**, 034022 (2018).

[16] S.-Y. Lee, M. Niethammer, and J. Wrachtrup, Phys. Rev. B **92**, 115201 (2015).

[17] H. Kraus, V. A. Soltamov, F. Fuchs, D. Simin, A. Sperlich, P. G. Baranov, G. V. Astakhov, and V. Dyakonov, Sci. Rep. **4**, 5303 (2014).

[18] D. Simin, V. A. Soltamov, A. V. Poshakinskiy, A. N. Anisimov, R. A. Babunts, D. O. Tolmachev, E. N. Mokhov, M. Trupke, S. A. Tarasenko, A. Sperlich, P. G. Baranov, V. Dyakonov, and G. V. Astakhov, Phys. Rev. X **6**, 031014 (2016).

[19] D. Simin, F. Fuchs, H. Kraus, A. Sperlich, P. G. Baranov, G. V. Astakhov, and V. Dyakonov, Phys. Rev. Appl. **4**, 014009 (2015).

[20] M. Niethammer, M. Widmann, S.-Y. Lee, P. Stenberg, O. Kordina, T. Ohshima, N. T. Son, E. Janzén, and J. Wrachtrup, Phys. Rev. Appl. **6**, 034001 (2016).

[21] C. J. Cochrane, J. Blacksberg, M. A. Anders, and P. M. Lenahan, Sci. Rep. **6**, 37077 (2016).

[22] A. N. Anisimov, D. Simin, V. A. Soltamov, S. P. Lebedev, P. G. Baranov, G. V. Astakhov, and V. Dyakonov, Sci. Rep. **6**, 33301 (2016).
[23] N. Mizuochi, S. Yamasaki, H. Takizawa, N. Morishita, T. Ohshima, H. Itoh, and J. Isoya, Phys. Rev. B **66**, 235202 (2002).
[24] N. Mizuochi, S. Yamasaki, H. Takizawa, N. Morishita, T. Ohshima, H. Itoh, and J. Isoya, Phys. Rev. B **68**, 165206 (2003).
[25] N. Mizuochi, S. Yamasaki, H. Takizawa, N. Morishita, T. Ohshima, H. Itoh, T. Umeda, and J. Isoya, Phys. Rev. B **72**, 235208 (2005).
[26] E. Janzén, A. Gali, P. Carlsson, A. Gällström, B. Magnusson, and N. Son, Phys. B **404**, 4354 (2009).
[27] N. T. Son, P. Stenberg, V. Jokubavicius, T. Ohshima, J. U. Hassan, and I. G. Ivanov, J. Phys.: Condens. Matter **31**, 195501 (2019).
[28] H. J. von Bardeleben, J. L. Cantin, I. Vickridge, and G. Battistig, Phys. Rev. B **62**, 10126 (2000).
[29] V. A. Soltamov, B. V. Yavkin, D. O. Tolmachev, R. A. Babunts, A. G. Badalyan, V. Y. Davydov, E. N. Mokhov, I. I. Proskuryakov, S. B. Orlinskii, and P. G. Baranov, Phys. Rev. Lett. **115**, 247602 (2015).
[30] V. Ivády, J. Davidsson, N. T. Son, T. Ohshima, I. A. Abrikosov, and A. Gali, Phys. Rev. B **96**, 161114(R) (2017).
[31] J. Davidsson, V. Ivády, R. Armiento, T. Ohshima, N. T. Son, A. Gali, and I. A. Abrikosov, Appl. Phys. Lett. **114**, 112107 (2019).
[32] I. G. Ivanov, C. Hallin, A. Henry, O. Kordina, and E. Janzén, J. Appl. Phys. **80**, 3504 (1996).
[33] T. A. G. Eberlein, C. J. Fall, R. Jones, P. R. Briddon, and S. Öberg, Phys. Rev. B **65**, 184108 (2002).
[34] R. Kuate Defo, X. Zhang, D. Bracher, G. Kim, E. Hu, and E. Kaxiras, Phys. Rev. B **98**, 104103 (2018).
[35] J. Heyd, G. E. Scuseria, and M. Ernzerhof, J. Chem. Phys. **118**, 8207 (2003).
[36] J. P. Perdew, K. Burke, and M. Ernzerhof, Phys. Rev. Lett. **77**, 3865 (1996).
[37] P. E. Blöchl, Phys. Rev. B **50**, 17953 (1994).
[38] G. Kresse and J. Furthmüller, Phys. Rev. B **54**, 11169 (1996).
[39] V. Ivády, T. Simon, J. R. Maze, I. A. Abrikosov, and A. Gali, Phys. Rev. B **90**, 235205 (2014).
[40] D. J. Tozer and N. C. Handy, Phys. Chem. Chem. Phys. **2**, 2117 (2000).
[41] A. Gali, E. Janzén, P. Deák, G. Kresse, and E. Kaxiras, Phys. Rev. Lett. **103**, 186404 (2009).
[42] C. Freysoldt, J. Neugebauer, and C. G. Van de Walle, Phys. Rev. Lett. **102**, 016402 (2009).
[43] M. J. Rayson and P. R. Briddon, Phys. Rev. B **77**, 035119 (2008).
[44] X. T. Trinh, K. Szász, T. Hornos, K. Kawahara, J. Suda, T. Kimoto, A. Gali, E. Janzén, and N. T. Son, Phys. Rev. B **88**, 235209 (2013).
[45] D. M. Martin, H. Kortegaard Nielsen, P. Lévêque, A. Hallén, G. Alfieri, and B. G. Svensson, Appl. Phys. Lett. **84**, 1704 (2004).
[46] T. Hornos, A. Gali, and B. G. Svensson, in *Silicon Carbide and Related Materials 2010*, Materials Science Forum Vols. 679–680 (Trans Tech, Baech SZ, Switzerland, 2011), pp. 261–264.
[47] M. E. Bathen, A. Galeckas, J. Müting, H. M. Ayedh, U. Grossner, J. Coutinho, Y. K. Frodason, and L. Vines, npj Quantum Inf. **5**, 111 (2019).
[48] L. Torpo, M. Marlo, T. E. M. Staab, and R. M. Nieminen, J. Phys.: Condens. Matter **13**, 6203 (2001).
[49] T. Kobayashi, K. Harada, Y. Kumagai, F. Oba, and Y.-i. Matsushita, J. Appl. Phys. **125**, 125701 (2019).